Spin- and valley-dependent negative magnetoresistance in a ferromagnetic MoS$_2$ junction with a quantum well

Wei-Tao Lu,[1,*] Hong-Yu Tian,[1] Hong-Mei Liu,[1] Yun-Fang Li,[2] and Wen Li[1]

[1]*School of Physics and Electronic Engineering, Linyi University, 276005 Linyi, China*
[2]*School of Mechanical & Vehicle Engineering, Linyi University, 276005 Linyi, China*

We studied the spin and valley transports and magnetoresistance effect in a MoS$_2$ junction with a quantum well inserted between the gate voltage and the ferromagnetic MoS$_2$, which can apply generally to other transition metal dichalcogenides with the same crystal structure. In the absence of a quantum well, the broken inversion symmetry and spin-orbit coupling for MoS$_2$ could give rise to a fully spin- and valley-polarized conductance for the parallel configuration, while there is no spin and valley polarization for the antiparallel configuration. The general condition of pure polarization and the position of resonant conductance are achieved. The magnetoresistance is positive and oscillates with the gate voltage. Dramatically, the presence of a quantum well can lead to the formation of spin-polarized quantum well states. As a result, the conductances for opposite spin and valley indices have a steady phase shift, making them oscillate in antiphase with the well width. Therefore, the high spin and valley polarization could be obtained for the antiparallel and parallel configurations. In particular, the spin-polarized quantum well states directly result in negative polarization and negative magnetoresistance.

I. INTRODUCTION

Manipulation of spin and valley degrees of freedom is an important topic of condensed matter physics and a key step toward realizing novel quantum technologies. As a promising candidate to realize the spintronics and valleytronics, recently, two-dimensional materials and particularly the transition metal dichalcogenides (TMDs) have attracted much attention [1–3]. The family of TMDs (e.g., MX_2; $M =$ Mo and W; $X =$ S, Se, and Te) represents a new class of two-dimensional semiconductors with a large direct band gap [4,5]. There are two inequivalent valleys K and K' located at the corners of the hexagonal Brillouin zone, similar to graphene. Distinctively, TMDs have inherently broken inversion symmetry and strong spin-orbit coupling [6], leading to a spin-valley locking relationship, where the spin splitting of the valence bands is opposite at the two valleys due to a time-reversal symmetry [2,7–9]. TMDs provide an ideal platform to study the rich spin and valley dynamics.

The monolayer MoS$_2$ is a typical TMD with spin-orbit coupling of 150 meV and band gap of 1.66 eV [7]. A MoS$_2$ transistor with room-temperature mobility of at least 200 cm^2 V^{-1} s^{-1} has been fabricated using a hafnium oxide gate dielectric [10]. It has been demonstrated that the valley degree of freedom in MoS$_2$ can be efficiently controlled by the optical [4,7,11–13], electrical [14–16], and magnetic [17,18] techniques, resulting in novel physics and optoelectronic application. Because of spin-orbit coupling and orbital asymmetry, the unconventional quantum Hall effect [19] and quantum spin Hall effect [20] are predicted in MoS$_2$ through its band structure. The magnetic field perpendicular to MoS$_2$ could significantly enhance the spin splitting in the conduction band

and lead to a beating of the Shubnikov–de Haas oscillations [21,22]. Valley- and spin-switch effects are suggested in the ferromagnetic/superconducting/ferromagnetic MoS$_2$ junction, at the interface of which the Andreev reflection occurs [23]. Furthermore, the valley and spin transport can be electrically manipulated by a gate voltage in a normal/ferromagnetic/normal MoS$_2$ junction device [24,25]. In experiment, quantum transport measurement of MoS$_2$ has been performed using a van der Waals heterostructure device platform [26].

On the other hand, there is a strong interest in the tunneling magnetoresistance (TMR) of magnetic tunnel junctions due to its application in digital storage and magnetic sensor technologies [27]. The TMR effect is concerned with the electrode controlled different currents under different magnetizations. Recently, the transport and TMR effect through a ferromagnetic/insulating/ferromagnetic (F/I/F) junction have been studied in graphene [28], silicene [29], and phosphorene [30]. Interestingly, the charge conductance in phosphorene can attain a minimum (or maximum) at the parallel (or antiparallel) configuration in the F/I/F structure with a p-doped I region [30]. In this article, we propose a type of junction in TMDs, i.e., the ferromagnetic/insulating/normal/ferromagnetic (F/I/N/F) junction [see Fig. 1(a)]. Without loss of generality, we choose the model of MoS$_2$ for a concrete discussion. Different from an F/I/F junction, an N region is inserted between the I and F regions in the F/I/N/F junction, and so the structure becomes asymmetric. We find that the N region could behave as a quantum well for a certain spin, leading to the formation of spin-polarized quantum well states, which greatly affects the spin and valley conductances and TMR in MoS$_2$, such as the negative valley polarization and negative magnetoresistance. In addition, due to the broken inversion symmetry and strong spin-orbit coupling, the result of MoS$_2$ differs from that of graphene and silicene [28,29].
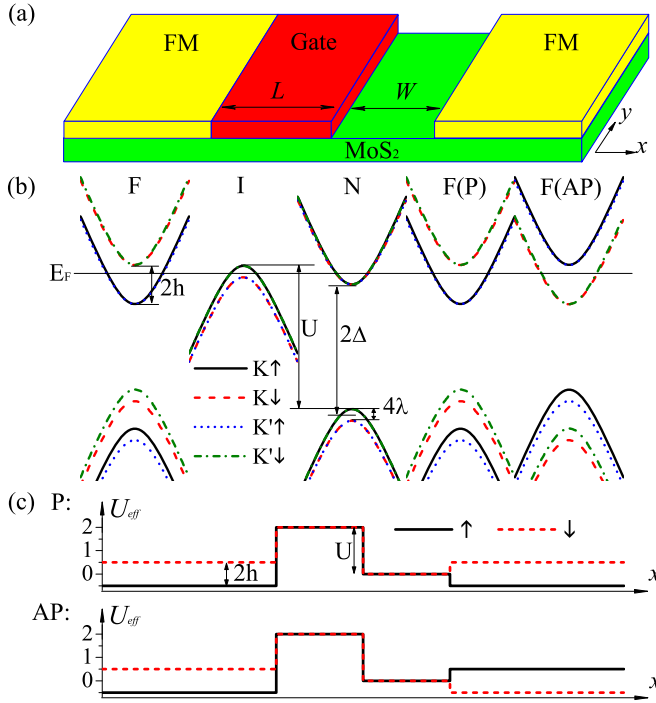
*luweitao@lyu.edu.cn

FIG. 1. (a) Schematic diagram of MoS$_2$-based F/I/N/F junction. (b) Band structure near Dirac points. The horizontal line denotes the Fermi energy E_F. (c) The effective potential $U_{eff}(x) = U(x) - s_z h(x)$ for spin-up and spin-down electrons in the P and the AP configurations.

The paper is organized as follows. In Sec. II we present the theoretical model and formulation. The numerical results on spin and valley polarizations and TMR in the F/I/N/F junction are shown in Sec. III. Finally, we draw conclusions in Sec. IV.

II. THEORETICAL FORMULATION

The electronic structure of MoS$_2$ has been studied in the framework of *ab initio* and tight-binding calculations [31,32]. Although the band structure of MoS$_2$ is complex, the low-energy electronic behavior could be understood within an effective two-band model [7], which is confirmed by first-principles calculations and could well describe the optical properties of the TMD family in experiments [11–13]. The considered F/I/N/F junction in MoS$_2$ is shown in Fig. 1(a). The left and right ferromagnetic electrodes can be induced via the magnetic proximity effect [33,34] or magnetic doping [35]. The insulating tunnel barrier with width L can be realized by a local gate voltage, and the induced electric field is perpendicular to MoS$_2$ sheet. The first-principles calculation implies that the Jahn-Teller distortion of the lattice structure induced by the electric field is quite weak, and so its influence is neglected (see the Appendix). The width of normal MoS$_2$ is W. The electrons and holes in the vicinity of the two valleys K and K' of MoS$_2$ and other TMDs are well described by massive Dirac fermions. Thus, the low-energy Hamiltonian for the proposed junction can be written as [7,8]

$$H = \hbar v_F (k_x \tau_z \sigma_x + k_y \sigma_y) + \Delta \sigma_z + (\lambda \tau_z s_z - \lambda \tau_z s_z \sigma_z)$$
$$+ U(x) - s_z h(x), \quad (1)$$

where $v_F = 5.3 \times 10^5$ m/s is the Fermi velocity, $\sigma_{x,y,z}$ are Pauli matrices, $2\Delta = 1.66$ eV is the band gap, and $4\lambda = 150$ meV is the spin-orbit coupling [7]. $\tau_z = \pm 1$ stands for the K and K' valleys. $s_z = \pm 1$ stands for spin-up and spin-down states. The tunnel barrier $U(x) = U\Theta(x)\Theta(L - x)$, and $\Theta(x)$ is the Heaviside step function. The exchange splitting in the two electrodes $h(x) = h[\Theta(-x) \pm \Theta(x - L - W)]$, where the signs $\pm$ correspond to the parallel (P) and the antiparallel (AP) configurations of magnetization, respectively. The exchange field h and spin-orbit coupling λ define the energies of band edges for different spins at two valleys.

The eigenvalues of the Hamiltonian are given by

$$E_\pm = U_{\tau s} \pm \sqrt{\Delta_{\tau s}^2 + (\hbar v_F k_F)^2}, \quad (2)$$

with $U_{\tau s} = \lambda \tau_z s_z + U(x) - s_z h(x)$ and $\Delta_{\tau s} = \Delta - \lambda \tau_z s_z$. k_F is the momentum. Due to the translational invariance in the y direction, the transverse wave vector k_y is conserved, and the eigenstate has the form

$$\psi(x) = a \begin{pmatrix} 1 \\ \frac{\hbar v_F k_+}{E_F - U_{\tau s} + \Delta_{\tau s}} \end{pmatrix} e^{iqx} + b \begin{pmatrix} 1 \\ \frac{-\hbar v_F k_-}{E_F - U_{\tau s} + \Delta_{\tau s}} \end{pmatrix} e^{-iqx}, \quad (3)$$

where $k_\pm = \tau_z q \pm i k_y$ and q requires $q^2 = [(E_F - U_{\tau s})^2 - \Delta_{\tau s}^2]/(\hbar v_F)^2 - k_y^2$. The transmission probability $T_{\tau s}$ can be calculated using the transfer matrix technique. According to the Landauer-Büttiker formula, the conductance for a particular spin in a particular valley at zero temperature is given by

$$G_{\tau s} = \frac{e^2}{h} \int_{-k_F}^{k_F} T_{\tau s} \frac{dk_y}{2\pi/L_y}$$

$$= G_0 \frac{\sqrt{(E_F - \lambda \tau_z s_z + s_z h)^2 - \Delta_{\tau s}^2}}{E_F}$$

$$\times \int_{-\pi/2}^{\pi/2} T_{\tau s} \cos\theta \, d\theta, \quad (4)$$

where θ is the incident angle with respect to the x direction. $G_0 = e^2 L_y E_F / (2\pi h \hbar v_F)$ is taken as the conductance unit, and L_y is the sample size along the y direction. The spin and valley resolved conductances are defined as $G_{\uparrow(\downarrow)} = (G_{K\uparrow(\downarrow)} + G_{K'\uparrow(\downarrow)})/2$ and $G_{K(K')} = (G_{K(K')\uparrow} + G_{K(K')\downarrow})/2$, respectively. Then we introduce the spin polarization P_s and valley polarization P_v:

$$P_s = (G_\uparrow - G_\downarrow)/(G_\uparrow + G_\downarrow), \quad (5)$$

$$P_v = (G_K - G_{K'})/(G_K + G_{K'}). \quad (6)$$

The total conductance $G = G_\uparrow + G_\downarrow = G_K + G_{K'}$, which is labeled as G_P and G_{AP} for the P and the AP configurations, respectively. The TMR can be defined as

$$\text{TMR} = (G_P - G_{AP})/G_P. \quad (7)$$

Before proceeding with the calculations, we discuss the band structure and the effective potential, as shown in Figs. 1(b) and 1(c), respectively. In the normal MoS$_2$, the spin splitting is opposite at different valleys in the valence band, which plays a key role to the realization of spin and valley polarizations. In both ferromagnetic (FM) electrodes, the exchange field h

lifts the spin degeneracy in the conduction band, and the spin splitting has the same direction at both valleys [see Fig. 1(b)]. Therefore, the valley polarization is coupled to the spin polarization in the proposed junction. In order to utilize such a specific valence band, we use the gate voltage U to tune the Fermi level locally. In the tunnel barrier, when the Fermi energy E_F satisfies $E_F > U + \Delta$, E_F crosses the conduction band, and all of $K \uparrow$, $K \downarrow$, $K' \uparrow$, and $K' \downarrow$ electronic states are degenerate. When $U - \Delta + 2\lambda\tau_z s_z < E_F < U + \Delta$, E_F is located inside the band gap, and no state exists in the barrier. When $E_F < U - \Delta + 2\lambda\tau_z s_z$, E_F crosses the valence band, where the states are nondegenerate. Particularly, when $U - \Delta - 2\lambda < E_F < U - \Delta + 2\lambda$, only $K \uparrow$ and $K' \downarrow$ states exist, but all states exist at $E_F < U - \Delta - 2\lambda$. In both electrodes, the critical value is $E_c = \Delta - s_z h$ in conduction band. For the P configuration, all states exist at $E_F > \Delta + h$, only spin-up states exist at $\Delta - h < E_F < \Delta + h$, and no state exists at $E_F < \Delta - h$. For the AP configuration, due to the antisymmetry of band structures between the left and right electrodes, at $\Delta - h < E_F < \Delta + h$, spin-up (or spin-down) states only exist in the left (or right) electrodes, and so no transport exists. In addition, Fig. 1(c) displays the profile of the effective potential $U_{\text{eff}}(x) = U(x) - s_z h(x)$ that the spin-up and spin-down electrons experience in the P and the AP configurations. Observably, there is a quantum well for spin-down (or spin-up) electrons in the P (or the AP) configuration. The spin-polarized quantum well states can be formed in the N region, leading to enhancement of electron tunneling [36]. Therefore, the band structure and potential field can be regulated by the ferromagnet and gate voltage, which strongly modulate the transport feature.

III. RESULTS AND DISCUSSIONS

In this section we present the numerical results for the F/I/N/F junction in MoS₂. Considering the validity of the continuum model described in Eq. (1), the corresponding parameters should be chosen. Throughout the paper, we set the Fermi energy $E_F = 1.2\Delta$, restrict the exchange field in the range $0.0 \leqslant h \leqslant 0.21\Delta$, and restrict the electrostatic potential in the range $2.0\Delta \leqslant U \leqslant 2.6\Delta$, so all the discussions are mainly in the low-energy region, which can ensure the validity of the model and the negligible effect of high-energy orbitals (see the Appendix). Δ is the unit for E_F, U, and h. $k_0 = E_F/\hbar v_F$ is the unit for L and W. G_0 is the unit for $G_{\tau s}$.

A. In the absence of a quantum well ($W = 0$)

First, we discuss the case of $W = 0$, i.e., without normal MoS₂, and the model returns to the F/I/F junction. Figure 2 shows the conductance $G_{\tau s}$ as a function of barrier width L in the P [Figs. 2(a)–2(d)] and AP [Figs. 2(e) and 2(f)] configurations. For the P configuration, at $h = 0.1$ and $U = 2.5$ in Fig. 2(a), satisfying $\Delta + h < E_F < U - \Delta - 2\lambda$, the Fermi energy E_F crosses the bands for both spins near both valleys in F and I regions, and so all electrons can tunnel through the junction. All conductances oscillate damply with L, the fashions of which are distinct for both spins at both valleys. The resonant conductance arises from the Fabry-Pérot interference effect of incident electron in the I region. In fact,
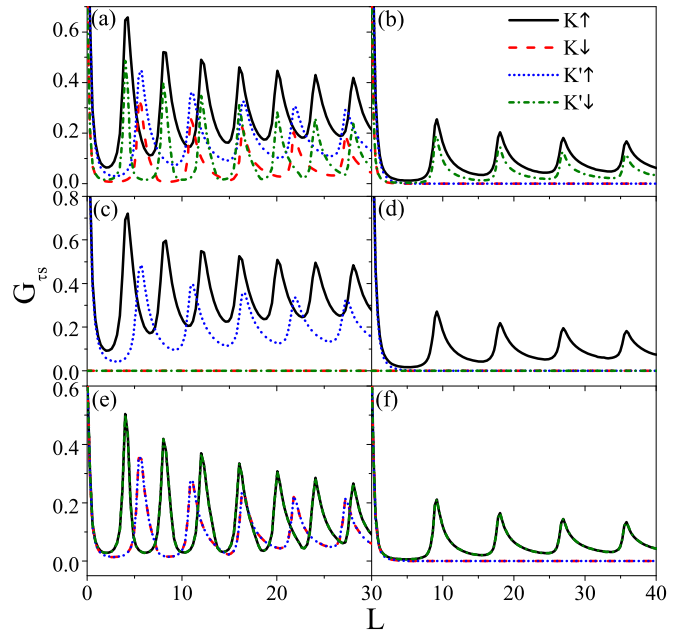

FIG. 2. Conductance $G_{\tau s}$ versus L for (a)–(d) the P and (e)–(f) the AP configurations. $h = 0.1$ and $U = 2.5$ in (a) and (e); $h = 0.1$ and $U = 2.2$ in (b) and (f); $h = 0.21$ and $U = 2.5$ in (c); $h = 0.21$ and $U = 2.2$ in (d).

the I region, i.e., the potential barrier, could be regarded as a one-dimensional Fabry-Pérot interferometer, where the cavity is the region inside the barrier. The incident wave would suffer multiple reflections between the two interfaces of the barrier and interfere with itself. The Fabry-Pérot resonances could occur with constructive interference, where the transmission $T_{\tau s} = 1$ at resonance condition $qL = m\pi$. Combining with the relation $q^2 = [(E_F - U_{\tau s})^2 - \Delta_{\tau s}^2]/(\hbar v_F)^2 - k_y^2$, we can obtain the width L_m where the resonant conductance takes place,

$$L_m = m\pi/k_F$$
$$= m\pi\hbar v_F/\sqrt{(E_F - U - \lambda\tau_z s_z)^2 - (\Delta - \lambda\tau_z s_z)^2}. \quad (8)$$

k_F is the momentum in the I region and m is an integer. Thus, $G_{K\uparrow}$ (or $G_{K\downarrow}$) and $G_{K'\downarrow}$ (or $G_{K'\uparrow}$) take on the same oscillation period. For given E_F, the average value of $G_{K\uparrow}$ is larger due to the broad crossed band, while the average value of $G_{K\downarrow}$ is smaller due to the narrow crossed band [see Fig. 1(b)]. Because of the opposite spin splitting of valence band near the K and K' valleys, when $\Delta + h < E_F$ and $U - \Delta - 2\lambda < E_F < U - \Delta + 2\lambda$, $G_{K\uparrow}$ and $G_{K'\downarrow}$ still exist, while $G_{K\downarrow}$ and $G_{K'\uparrow}$ are suppressed and decay exponentially with L [see Fig. 2(b)]. Utilizing the spin splitting induced by h, when $\Delta - h < E_F < \Delta + h$ and $E_F < U - \Delta - 2\lambda$, only $G_{K\uparrow}$ and $G_{K'\uparrow}$ exist [see Fig. 2(c)]. Accordingly, one can conclude that the incoming quasiparticles from the left F region at $\Delta - h < E_F < \Delta + h$ and $U - \Delta - 2\lambda < E_F < U - \Delta + 2\lambda$ are completely dominated by the spin-up electrons from the K valley, since only $G_{K\uparrow}$ exists [see Fig. 2(d)]. This means that it is possible to achieve a current with specific spin and valley indices by adjusting U and h in the P configuration. However, in the AP configuration, because both band structures and
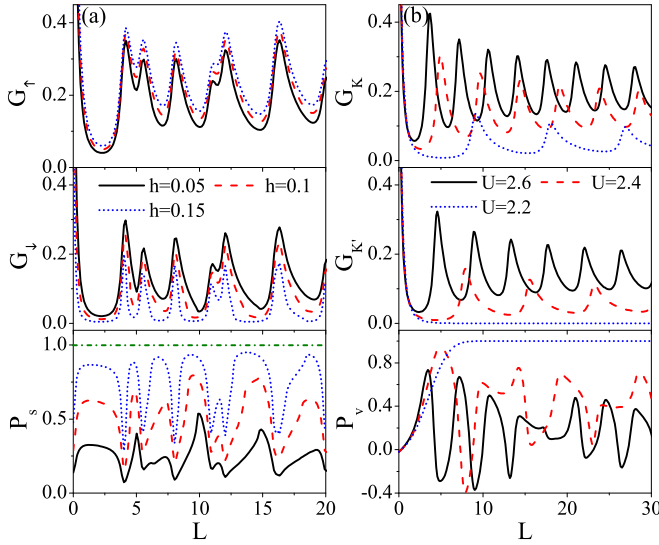
FIG. 3. For the P configuration: (a) spin conductance $G_{\uparrow,\downarrow}$ and spin polarization P_s versus L at $U = 2.5$, where the curves are for $h = 0.05$, 0.1, and 0.15; (b) valley conductance $G_{K,K'}$ and valley polarization P_v versus L at $h = 0.21$, where the curves are for $U = 2.6$, 2.4, and 2.2.

FIG. 4. Total conductance $G_{P,AP}$ and TMR versus U at $L = 15$, for $h = 0.1$, 0.15, and 0.19.

potential fields are antisymmetric for $K \uparrow$ (or $K \downarrow$) and $K' \downarrow$ (or $K' \uparrow$) electrons due to the symmetric structure of F/I/F junction [see Figs. 1(b) and 1(c)], $G_{K\uparrow} = G_{K'\downarrow}$ and $G_{K\downarrow} = G_{K'\uparrow}$ [see Fig. 2(e)]. $G_{K\downarrow}$ and $G_{K'\uparrow}$ can be suppressed by tuning the Fermi level in the I region [see Fig. 2(f)]. Obviously, the spin and valley polarization is zero, that is, $P_s = P_v = 0$ at $W = 0$ in the AP configuration.

In Fig. 3, we present spin conductance $G_{\uparrow,\downarrow}$, spin polarization P_s, valley conductance $G_{K,K'}$, and valley polarization P_v as functions of L for the P configuration. Due to the different oscillation periods of $G_{\tau s}$, the oscillating behaviors of $G_{\uparrow,\downarrow}$ and P_s are a superposition of two periods [see Fig. 3(a)]. Because of the spin filtering effect of the ferromagnetic electrode, as h increases, $G_{\uparrow}$ increases but $G_{\downarrow}$ decreases gradually, leading to a high spin polarization. When $h > E_F - \Delta$, $G_{\downarrow}$ decreases to zero, and a full spin polarization with $P_s = 1$ is obtained. Note that $P_s = -1$ when $h < \Delta - E_F$. At $h = 0.21$ in Fig. 3(b), satisfying $h > E_F - \Delta$, valley conductance $G_{K(K')}$ is mainly afforded by $G_{K(K')\uparrow}$. As U decreases, both $G_{K'}$ and G_K decrease, while their oscillation periods become large, which can be explained by Eq. (8). We can confirm that when U and h satisfy the condition

$$E_F + \Delta - 2\lambda < U < E_F + \Delta + 2\lambda, \quad |h| > E_F - \Delta, \quad (9)$$

$G_{K'}$ can be suppressed for large L, and only G_K exists, resulting in a fully valley-polarized conductance.

Figure 4 shows the total conductances G_P and G_{AP} for the P and the AP configurations, and TMR as a function of U. The conductance is weak in the region $U < E_F + \Delta + 2\lambda$, since only $K \uparrow$ and $K' \downarrow$ electrons could pass through the junction. Both conductance and TMR oscillate with U. The oscillation periods and phases for G_P and G_{AP} are nearly the same. As h increases, G_{AP} is greatly restrained, while G_P is almost invariant, resulting in the increase of TMR. When $|h| > E_F -$
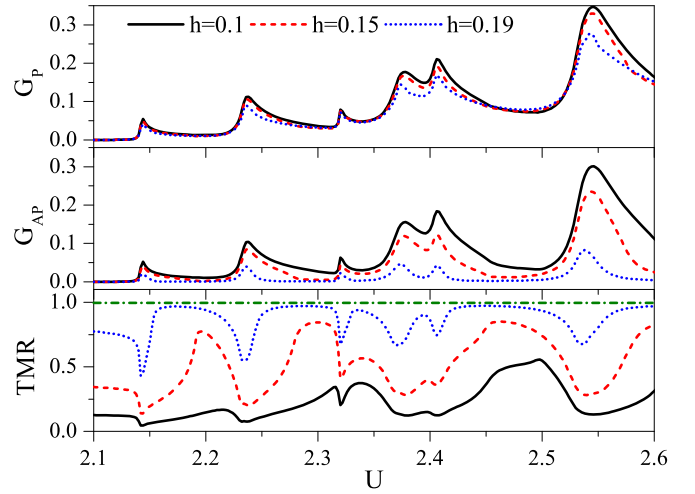
$\Delta = 0.2$, $G_{AP} = 0$ and one can get a positive TMR with TMR $= 1$.

It should be noted that although the F/I/F junction has been studied in graphene and silicene, different results and physical mechanisms are obtained in MoS$_2$ due to the broken inversion symmetry and large band gap. The spin polarization in graphene was arrived at by the exchange splitting, but the valley degree of freedom always remains degenerate [28]. The band gap of silicene can be controlled by a field-induced staggered sublattice potential due to its buckled structure, which could be used to realize spin and valley polarizations [29]. Contrary to graphene and silicene, in MoS$_2$, a perfect spin and valley polarization could be obtained by adjusting the potential barrier due to the opposite spin splitting of the valence bands at the two valleys. Furthermore, it is difficult to observe the negative TMR effect in a MoS$_2$-based F/I/F junction due to the large band gap.

B. In the presence of a quantum well ($W \neq 0$)

In this section, we discuss transport through the F/I/N/F junction ($W \neq 0$) in a two-dimensional material. In contrast to that in an F/I/F junction, the oscillating behavior of conductance becomes abundant, due to the combining effect of the Fabry-Pérot interference effect and the spin-polarized quantum well states. Figure 5 displays the conductance $G_{\tau s}$ as a function of well width W for the P and AP configurations. It is seen clearly that the conductances for both configurations are oscillating functions of W. The amplitudes and periods of oscillations depend sensitively on the spin and valley indices. One can find a few prominent features for the conductance:

(1) For the P configuration in Fig. 5(a), the amplitude of $G_{K(K')\downarrow}$ ($G_{K(K')\uparrow}$) is larger (smaller), and the position of $W = 0$ is the nadir (peak) of $G_{K(K')\downarrow}$ ($G_{K(K')\uparrow}$). The reason is that the N region in the junction acts as a quantum well (or step) for spin-down (or spin-up) electrons for the P configuration [see Fig. 1(c)]. The formation of spin-polarized quantum well states would lead to resonant tunneling. The resonance occurs
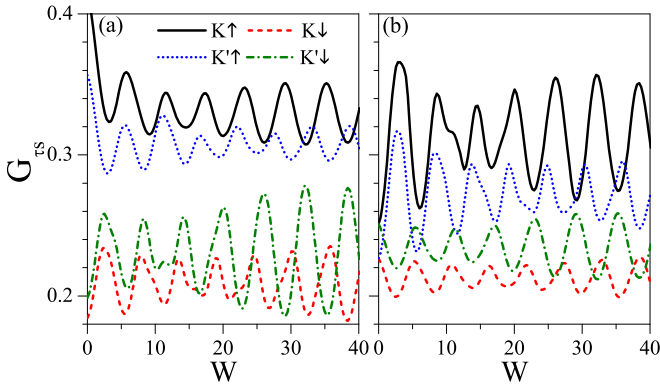
FIG. 5. Conductance $G_{\tau s}$ versus W for (a) the P and (b) the AP configurations at $h = 0.1$, $U = 2.6$, and $L = 18$.

when the Fermi energy consists with the energy level of a quasibound state in the quantum well, which strongly depends on the well width W. The oscillation period T_W can be given approximately by

$$T_W = \pi \hbar v_F / \sqrt{(E_F - \lambda \tau_z s_z)^2 - (\Delta - \lambda \tau_z s_z)^2}, \quad (10)$$

which is not exact enough due to the effect of the potential barrier. Since the quantum well is shallow, the resonant enhancement of the conductance $G_{K(K')\downarrow}$ is not sufficiently obvious. However, the step potential for spin-up electrons would destroy the Fabry-Pérot interference, and lead to the suppression of conductance $G_{K(K')\uparrow}$.

(2) For the AP configuration in Fig. 5(b), due to the asymmetry of the F/I/N/F junction, $G_{K\uparrow}$ ($G_{K\downarrow}$) is no longer equal to $G_{K'\downarrow}$ ($G_{K'\uparrow}$). Thus, the spin and valley polarization could be expected in the AP configuration at $W \neq 0$. Contrary to the P configuration, because of the quantum well (step) for spin-up (spin-down) electrons in the N region, the amplitude of $G_{K(K')\uparrow}$ ($G_{K(K')\downarrow}$) is larger (smaller), and its average value is greater (less) than the value at $W = 0$.

(3) Most importantly, for both configurations, from Eq. (10) one can find that $G_{K\uparrow}$ ($G_{K\downarrow}$) and $G_{K'\downarrow}$ ($G_{K'\uparrow}$) have the same oscillation period and exhibit a steady phase shift by a half period, which makes them oscillate almost in antiphase. Dramatically, the peak of $G_{K\uparrow}$ ($G_{K\downarrow}$) corresponds to the nadir of $G_{K'\downarrow}$ ($G_{K'\uparrow}$) and vice versa. The phase shift should be related to the different electronic states of the two spins in the N region. However, $G_{K\uparrow}$ ($G_{K\downarrow}$) and $G_{K'\uparrow}$ ($G_{K'\downarrow}$) have different oscillation periods.

(4) Last but not least, the oscillation period of $G_{\tau s}$ for the P configuration is the same as that of the corresponding $G_{\tau s}$ for the AP configuration and has inverse oscillatory phases. These striking characteristics could give rise to the spin and valley polarizations and the negative TMR effect.

Figure 6(a) presents the spin conductance $G_{\uparrow,\downarrow}$ and spin polarization P_s, and Fig. 6(b) presents the valley conductance $G_{K,K'}$ and valley polarization P_v as functions of W for the AP configuration. As expected, both types of polarization start from zero, i.e., there is no polarization for vanishing W. At $U = 2.2$ satisfying $U < E_F + \Delta + 2\lambda$, only $G_{K\uparrow}$ and $G_{K'\downarrow}$ exist which have the inverse phases. Consequently, $G_\uparrow = G_K = G_{K\uparrow}$, $G_\downarrow = G_{K'} = G_{K'\downarrow}$, and $P_s = P_v$
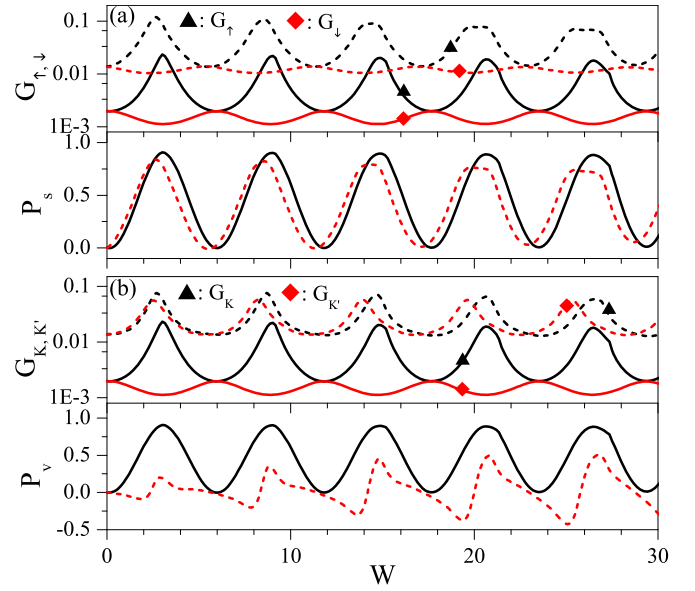

FIG. 6. (a) Spin conductance $G_{\uparrow,\downarrow}$ and spin polarization P_s and (b) valley conductance $G_{K,K'}$ and valley polarization P_v versus W for the AP configuration at $h = 0.18$ and $L = 25$. The solid and dashed curves are for $U = 2.2$ and 2.4, respectively.

oscillating periodically. When $U > E_F + \Delta + 2\lambda$, taking $U = 2.4$ for instance, all the electronic states are propagating modes and all channels are allowed. From Fig. 6(a) one can clearly see that $G_\uparrow$ and $G_\downarrow$ still have the same oscillation period with a inverse phase, and so a high spin polarization can be obtained which shows an oscillatory dependence on W. Whereas, as shown in Fig. 6(b), there is a simple phase shift between G_K and $G_{K'}$ with the increase of W, and their sizes are comparative, leading to a negative valley polarization, which can be understood based on the conductance in Fig. 5(b). The results indicate that a high spin and valley polarization can be achieved by virtue of a quantum well in the AP configuration, which is not observed in the F/I/F junction. In addition, the effect of a quantum well in the P configuration is similar to that in the AP configuration.

Finally, we discuss the TMR effect in the F/I/N/F junction, as shown in Fig. 7. Interestingly, the superposition of both spin conductances in both valleys leads to the comparable total conductances G_P and G_{AP} with well-defined oscillations. At $U = 2.2$ in Fig. 7(a), both G_P and G_{AP} oscillate with W, but the amplitude for the former is less than that for the latter. As a result, TMR oscillates periodically between positive and negative values, the decay of which is rather slow. Figures 7(b) and 7(c) display the contour plot of TMR(L, W) and TMR(U, W), respectively. One may find that the negative TMR mainly arises in the region $U < E_F + \Delta + 2\lambda$. It is possible to achieve a strong positive or negative TMR ratio by a proper tuning of the structure parameter. It is noteworthy that the negative TMR is induced by the spin-polarized quantum well states in the junction, and the physical mechanism is completely different from that observed in graphene and silicene [28,29], where the negative TMR stems from the change of the charge type in the right ferromagnetic electrode.
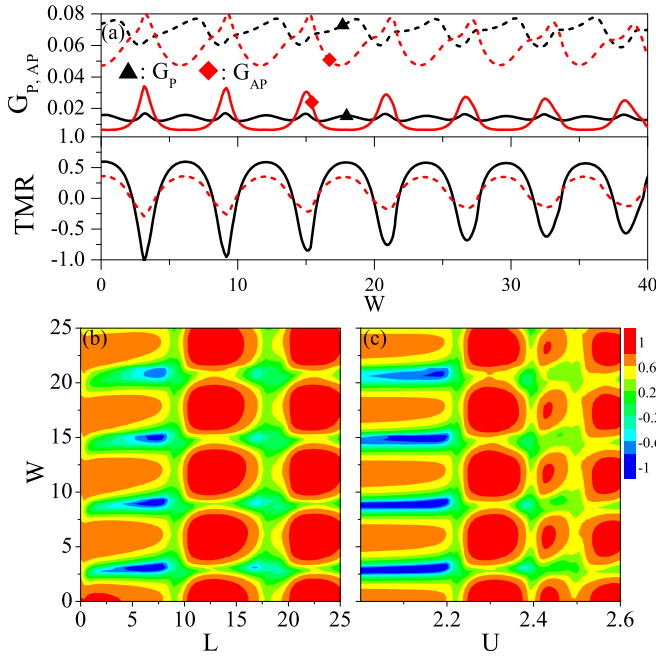
FIG. 7. (a) Total conductance $G_{P,AP}$ and TMR versus W at $h = 0.18$ and $U = 2.2$, where the solid and dashed curves are for $L = 8$ and 18, respectively. (b) Contour plot of TMR(L, W) at $U = 2.2$. (c) Contour plot of TMR(U, W) at $L = 8.0$.

IV. CONCLUSION

In summary, we proposed a type of junction in MoS_2, and studied the spin and valley polarizations and TMR through it. We found that the transport properties are sensitive to the band structure and the quantum well. Due to the broken inversion symmetry and spin-orbit coupling for MoS_2, a pure spin and valley polarization is achieved in the P configuration. Taking advantage of the spin-polarized quantum well states, the spin and valley polarization could also be obtained in the AP configuration. A strong negative TMR effect could be achieved by tuning the structure parameter. Valleytronics aims to generate and operate a highly polarized valley current. Recent experiments have demonstrated the local gate control of field-effect transistors based on monolayer and bilayer MoS_2 [10,15]. Our results imply that it is possible to achieve the gate regulation of valley-spin polarization and magnetoresistance in a MoS_2 tunnel junction device.

Note that the paper mainly studied the transport in an equilibrium system and assumed a short response time in the MoS_2 junction. In fact, the experimental works on TMDs demonstrated that the response time is in picosecond range [16,37]. First-principles calculations indicate that the electrons with different spins have the same Fermi velocity around K and K' points. Hence, the effect of nonsteady states in the response time should be quite little for the considered model. In addition, the main results of the paper arise from the broken inversion symmetry, strong spin-orbit coupling, and the spin-polarized quantum well states of the system. As we know, the physics in monolayers is essentially the same for all TMD families. Thus, the results are expected to be applicable also for other

TABLE I. Lattice structure of MoS_2 for different values of electric field E.

E (V/Å)	0.0	0.1	0.2	0.4	0.6	0.8
Mo-S bond (Å)	2.413/	2.413/	2.413/	2.413/	2.412/	2.412/
	2.413	2.413	2.413	2.413	2.414	2.414
S-S bond (Å)	3.127	3.127	3.127	3.127	3.128	3.129
∠ S-Mo-S (°)	80.79	80.79	80.79	80.79	80.80	80.81

TMD families, such as $MoSe_2$ and WS_2. The model could also provide a reference for controlling the electronic structure of other two-dimensional Dirac materials.

APPENDIX

Using first-principles calculations, the effect of the vertical electric field on the lattice structure and the energy band structure is discussed in Table I and Fig. 8, respectively. The band structure is calculated using the Vienna *ab initio* simulation package [38]. The exchange-correlation function is treated by the Perdew-Burke-Ernzerhof form within the generalized gradient approximation scheme [39]. The cutoff energy for plane waves is chosen to be 500 eV. A $(20 \times 20 \times 1)$ k-point mesh with Γ centered grid is used. The lattice constant of MoS_2 is 3.183 Å. The geometric structures of MoS_2 are fully relaxed with an electric field. From Table I we can see that as the electric field increases, the changes of both the bond length and the bond angle are less than 0.1%, implying that the distortion of the lattice structure of MoS_2 is very little. Figure 8 shows that the profile of the band structure is almost invariable with the electric field, except for the shift of the Fermi level along the energy axis. Near the Dirac points K and K', both the bottom of the conduction band and the top of the valence band are far away from other bands. This means that around K and K' points, only the highest valence band and the lowest
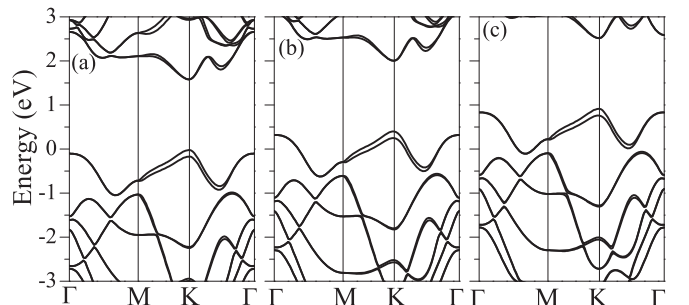

FIG. 8. Energy band structure of MoS_2 for different values of electric field E. $E = 0.0$, 0.2, and 0.8 V/Å in (a), (b), and (c), respectively.

conduction band can contribute to the transmission, and the effect of the high-energy orbital is quite small. Therefore, the considered model with an electric field can be described by Eq. (1) in the vicinity of the Dirac points.

[1] Q. H. Wang, K. Kalantar-Zadeh, A. Kis, J. N. Coleman, and M. S. Strano, Nat. Nanotechnol. **7**, 699 (2012).

[2] X. Xu, W. Yao, D. Xiao, and T. F. Heinz, Nat. Phys. **10**, 343 (2014).

[3] J. R. Schaibley, H. Yu, G. Clark, P. Rivera, J. S. Ross, K. L. Seyler, W. Yao, and X. Xu, Nat. Rev. Mater. **1**, 16055 (2016).

[4] A. Splendiani, L. Sun, Y. Zhang, T. Li, J. Kim, C.-Y. Chim, G. Galli, and F. Wang, Nano Lett. **10**, 1271 (2010).

[5] K. F. Mak, C. Lee, J. Hone, J. Shan, and T. F. Heinz, Phys. Rev. Lett. **105**, 136805 (2010).

[6] Z. Y. Zhu, Y. C. Cheng, and U. Schwingenschlögl, Phys. Rev. B **84**, 153402 (2011).

[7] D. Xiao, G. B. Liu, W. Feng, X. Xu, and W. Yao, Phys. Rev. Lett. **108**, 196802 (2012).

[8] H.-Z. Lu, W. Yao, D. Xiao, and S.-Q. Shen, Phys. Rev. Lett. **110**, 016806 (2013).

[9] R. Bertoni, C. W. Nicholson, L. Waldecker, H. Hubener, C. Monney *et al.*, Phys. Rev. Lett. **117**, 277201 (2016).

[10] B. Radisavljevic, A. Radenovic, J. Brivio, V. Giacometti, and A. Kis, Nat. Nanotechnol. **6**, 147 (2011).

[11] T. Cao, G. Wang, W. Han, H. Ye, C. Zhu, J. Shi, Q. Niu, P. Tan, E. Wang, B. Liu, and J. Feng, Nat. Commun. **3**, 887 (2012).

[12] K. F. Mak, K. He, J. Sahn, and T. F. Heinz, Nat. Nanotechnol. **7**, 494 (2012).

[13] H. Zeng, J. Dai, W. Yao, D. Xiao, and X. Cui, Nat. Nanotechnol. **7**, 490 (2012).

[14] S. Wu, J. S. Ross, G. Liu, G. Aivazian, A. Jones, Z. Fei, W. Zhu, D. Xiao, W. Yao, D. Cobden, and X. Xu, Nat. Phys. **9**, 149 (2013).

[15] J. Lee, K. F. Mak, and J. Shan, Nat. Nanotechnol. **11**, 421 (2016).

[16] Y. Ye, J. Xiao, H. Wang, Z. Ye, H. Zhu, M. Zhao, Y. Wang, J. Zhao, X. Yin, and X. Zhang, Nat. Nanotechnol. **11**, 598 (2016).

[17] T. Cai, S. A. Yang, X. Li, F. Zhang, J. Shi, W. Yao, and Q. Niu, Phys. Rev. B **88**, 115140 (2013).

[18] H. Rostami and R. Asgari, Phys. Rev. B **91**, 075433 (2015).

[19] X. Li, F. Zhang, and Q. Niu, Phys. Rev. Lett. **110**, 066803 (2013).

[20] M. A. Cazalilla, H. Ochoa, and F. Guinea, Phys. Rev. Lett. **113**, 077201 (2014).

[21] M. Tahir, P. Vasilopoulos, and F. M. Peeters, Phys. Rev. B **93**, 035406 (2016).

[22] M. Zubair, M. Tahir, P. Vasilopoulos, and K. Sabeeh, Phys. Rev. B **96**, 045405 (2017).

[23] L. Majidi and R. Asgari, Phys. Rev. B **90**, 165440 (2014).

[24] H. Li, J. Shao, D. Yao, and G. Yang, ACS Appl. Mater. Interfaces **6**, 1759 (2014).

[25] X. J. Qiu, Z. Z. Cao, Y. F. Cheng, and C. C. Qin, J. Phys.: Condens. Matter **29**, 105301 (2017).

[26] X. Cui, G.-H. Lee, Y. D. Kim, G. Arefe, P. Y. Huang *et al.*, Nat. Nanotechnol. **10**, 534 (2015).

[27] J. S. Moodera, L. R. Kinder, T. M. Wong, and R. Meservey, Phys. Rev. Lett. **74**, 3273 (1995).

[28] J. Zou, G. Jin, and Y. Ma, J. Phys.: Condens. Matter **21**, 126001 (2009).

[29] R. Saxena, A. Saha, and S. Rao, Phys. Rev. B **92**, 245412 (2015).

[30] M. Zare, L. Majidi, and R. Asgari, Phys. Rev. B **95**, 115426 (2017).

[31] S. Lebègue and O. Eriksson, Phys. Rev. B **79**, 115409 (2009).

[32] E. Cappelluti, R. Roldán, J. A. Silva-Guillén, P. Ordejón, and F. Guinea, Phys. Rev. B **88**, 075409 (2013).

[33] J. Qi, X. Li, Q. Niu, and J. Feng, Phys. Rev. B **92**, 121403(R) (2015).

[34] B. Scharf, G. Xu, A. Matos-Abiague, and I. Žutić, Phys. Rev. Lett. **119**, 127403 (2017).

[35] Y. C. Cheng, Q. Y. Zhang, and U. Schwingenschlögl, Phys. Rev. B **89**, 155429 (2014).

[36] A. Vedyayev, N. Ryzhanova, C. Lacroix, L. Giacomoni, and B. Dieny, Europhys. Lett. **39**, 219 (1997).

[37] P. Hein, A. Stange, K. Hanff, L. X. Yang, G. Rohde, K. Rossnagel, and M. Bauer, Phys. Rev. B **94**, 205406 (2016).

[38] G. Kresse and J. Hafner, Phys. Rev. B **47**, 558(R) (1993).

[39] J. P. Perdew, K. Burke, and M. Ernzerhof, Phys. Rev. Lett. **77**, 3865 (1996).